Research Square

Preprints are preliminary reports that have not undergone peer review.
They should not be considered conclusive, used to inform clinical practice,
or referenced by the media as validated information.

Hybrid PEO–hydrothermal–silane coating with synergistic Ce–8HQ inhibitor sealing for durable corrosion protection of AZ31 magnesium alloy

Majid Shahsanaei
University of Siegen
Nastaran Farahbakhsh
University of Siegen
Masoud Atapour
Isfahan University of Technology
Morteza Shamanian
Isfahan University of Technology
Benjamin Butz
University of Siegen
Christian Pritzel
University of Siegen
Manuela S. Killian
manuela.killian@uni-siegen.de
University of Siegen

Article

Keywords: Magnesium, PEO, Corrosion, Hydrothermal, Inhibitors, Hydrogen

Posted Date: May 6th, 2026

DOI: https://doi.org/10.21203/rs.3.rs-9486639/v1

License: This work is licensed under a Creative Commons Attribution 4.0 International License.
Read Full License

Additional Declarations: No competing interests reported.

Version of Record: A version of this preprint was published at npj Materials Degradation on October 13th, 2026. See the published version at https://doi.org/10.1038/s41529-026-00889-3.

Hybrid PEO–hydrothermal–silane coating with synergistic Ce–8HQ inhibitor sealing for durable corrosion protection of AZ31 magnesium alloy

Majid Shahsanaei [a, c], Nastaran Farahbakhsh [a], Masoud Atapour [b], Morteza Shamanian [b], Benjamin Butz [c], Christian Pritzel [a], and Manuela S. Killian [a]*

a) Chemistry and Structure of novel Materials, Department of Chemistry and Biology, University of Siegen, Paul-Bonatz-Str. 9-11, 57076 Siegen, Germany

b) Department of Materials Engineering, Isfahan University of Technology, Isfahan 84156-83111, Iran

c) Micro- and Nano Analytics Group, University of Siegen, Adolf-Reichwein-Straße 28, 57076 Siegen, Germany

* Corresponding author, Email: Manuela Killian, manuela.killian@uni-siegen.de

Abstract

Coatings with long-term corrosion protection capabilities have attracted considerable attention for enhancing the surface performance of magnesium (Mg) alloys in industrial applications. In this study, plasma electrolytic oxidation (PEO) coatings were further sealed using cerium (Ce) via hydrothermal treatment, followed by the application of a silane layer containing 8-hydroxyquinoline (8HQ). The results demonstrate a synergistic corrosion-inhibiting effect between Ce and 8HQ, resulting in nearly a 100-fold enhancement in corrosion resistance after 16 days of immersion in 3.5% NaCl. Additionally, the H_2 evolution rate was decreased by 80% compared to the unsealed PEO coating after 30 days of immersion.

Keywords

Magnesium; PEO; Corrosion; Hydrothermal; Inhibitors; Hydrogen

1. Introduction

The impaired resistance of Mg and its alloys to degradation is a significant limitation, despite their excellent mechanical properties [1,2]. Thermodynamically, Mg exhibits a low standard potential, making it highly reactive and this inherent property makes Mg susceptible to corrosion in aqueous environments or even when exposed to air [3]. Recently, organic-inorganic hybrid coatings have attracted considerable attention due to their effective combination of beneficial properties from both organic and inorganic components, offering a promising approach to enhance the corrosion resistance of Mg alloys [4,5].

Various coatings have been applied to Mg and its alloys to improve their corrosion resistance, including proteins [6], PEO [7], anodization [8], and layered double hydroxide (LDH) [9,10] which effectively create oxide layers on Mg substrates. The latter coatings offer significant protective benefits, enhancing the durability and performance of Mg-based materials in corrosive environments. Among the available techniques, the surface preparation of Mg alloys using the PEO process has proven highly effective for coating systems [11,12]. The micropores and microcracks formed during the PEO process create an ideal surface morphology for mechanical interlocking, significantly enhancing the adhesion strength of organic coatings to Mg substrates [13]. Additionally, various corrosion inhibitors, such as Ce [14] and lanthanum (La) [15], can be infused into these pores to provide active corrosion protection. Likewise, PEO has been widely used to fabricate superhydrophobic coatings by incorporating polymeric and silane-based materials with ceramic oxides, enhancing wettability and corrosion resistance [16]. Moreover, recent research on post-PEO hydrothermal (HT) treatment has gained attention for its effectiveness in sealing cracks and pores using corrosion inhibitors [17,18]. Zhang et al. [19,20] investigated the HT treatment of PEO-coated Mg alloy AZ31, focusing on the synthesis of layered double hydroxides (LDHs). They found that HT treatment with Al^{3+} solutions

significantly improved the corrosion resistance of phosphate- and silicate-based PEO coatings, with superior corrosion protection and self-healing ability attributed to the synergy between Ce species and phosphate.

Another approach is the functionalization of surfaces to improve the corrosion resistance of metal substrates and enhance the adhesion of top coatings such as functional or epoxy [21]. Several studies have shown that silane films can strengthen the bond between organic coatings and Mg substrates [22,23]. This method has been proven to significantly enhance the protective properties of the coatings. For instance, silane treatment greatly enhances the performance of Mg-rich primer applied to AZ91D alloy [24]. The silane layer modifies the surface and enhances the compatibility between the metal substrate and the polymer layers. This is accomplished by forming strong covalent bonds between the hydrolysable silicate groups and the substrate [25]. This process not only strengthens the adhesion of the organic layer but also improves its protective qualities [26]. Marcoen et al. [27] demonstrated that aminopropyl triethoxysilane enhances adhesion to low-carbon steel by forming hydrogen bonds, which convert into covalent Si–O–Fe bonds during curing at 50–75 °C, leading to improved coating performance. On the other hand, recent studies have focused on designing tailor-made silane mixtures with specific chemical properties and optimizing them by incorporating various additives and corrosion inhibitors to provide active corrosion protection or self-healing properties [13,28]. For instance, Su et al. [29] showed that combining tetraethyl orthosilicate (TEOS) with γ-glycidoxypropyltrimethoxysilane (GPTMS) effectively prevents crack formation and improves adhesion. Furthermore, adding Ce ions as a corrosion inhibitor enhances the corrosion resistance and self-healing properties of hot-dip galvanized steel.

This study aims to develop and evaluate advanced hybrid coatings by integrating different coating systems to create a PEO/HT/Silane coating with effective corrosion protection. Due to

their porous morphology, surface roughness, and free surface energy, PEO coatings have a strong potential for active corrosion properties through sealing with corrosion inhibitors [23,30]. Based on previous studies of Ce as a corrosion inhibitor for Mg-based materials, we selected it as the main component of the HT solution to seal the cracks and pores of the PEO coating [31–33]. By combining APTES and TEOS silanes, we aim to leverage the amine group for strong bonding while forming an inorganic network to enhance the barrier properties of the silane layer not only to improve corrosion protection but also to minimize the release of Ce from the sealed PEO. Besides investigating corrosion resistance, this study also evaluates the self-repairing ability after applying an epoxy topcoat in the presence of an artificial defect on PEO.

2. Materials and Methodes

2.1. Formation of PEO and HT coatings

To perform the PEO process, Mg AZ31 alloy samples with dimensions of 10 × 10 × 2.5 mm and a composition of Mg 96 wt%, Al 3 wt%, and Zn 1 wt% were surface polished using water abrasive sandpapers ranging from P800 to P4000 grit. The samples were then thoroughly cleaned by sonication in acetone and ethanol, followed by drying under a nitrogen stream. The PEO process was carried out in a setup with stainless steel as the cathode and Mg alloy as the anode, using a DC power source (600V, 10A), and an electrolyte composition of KOH (8 g/l), Na_2SiO_3 (6 g/l), and Na_3PO_4 (4 g/l) at a temperature of 15 °C with continuous stirring. The coating was formed under a constant 400V for 10 min.

Thereafter, the PEO-coated samples underwent HT treatment to seal the pores and cracks with Ce-containing oxide as a corrosion inhibitor. For this purpose, the samples were placed in an autoclave containing 100 mL of 0.1 mol/L $CeCl_3$ for a hydrothermal reaction at 120 °C for 75 min. Subsequently, the samples were rinsed with deionized water and dried to get the PEO/Ce sample.

2.2. Silan layer and 8-HQ

To coat the PEO/Ce samples with a silane layer, we used two types of silane: (3-aminopropyl) triethoxysilane (APTES) and tetraethoxysilane (TEOS), both from Sigma-Aldrich Co. We mixed them in a 50:50 ratio using water/ethanol (80:20) solvent system, with a silane/solution ratio of 30:70. To form organic complexes with metal alkoxides and improve the stability of the sol, the pH of the silane solution was adjusted to 5 by the dropwise addition of acetic acid [34]. To complete hydrolysis, the solution was kept overnight under continuous stirring. Then, the PEO/Ce samples were immersed in the solution and placed under vacuum for 2 min to assist to the sealing process. After removal from the silane solution, the samples were remained at room temperature for 24 h, the samples were annealed at 150°C for 3 h to complete curing and obtain PEO/Ce/Silane. To apply a silane layer containing the organic corrosion inhibitor, the same procedure was repeated, with the addition of 3g/L 8-HQ to the solution a few seconds after adjusting the pH, resulting in PEO/HT/Silane+8HQ. Figure 1 shows the schematic illustration of the preparation process of PEO/HT/Silane+8HQ composite coating.

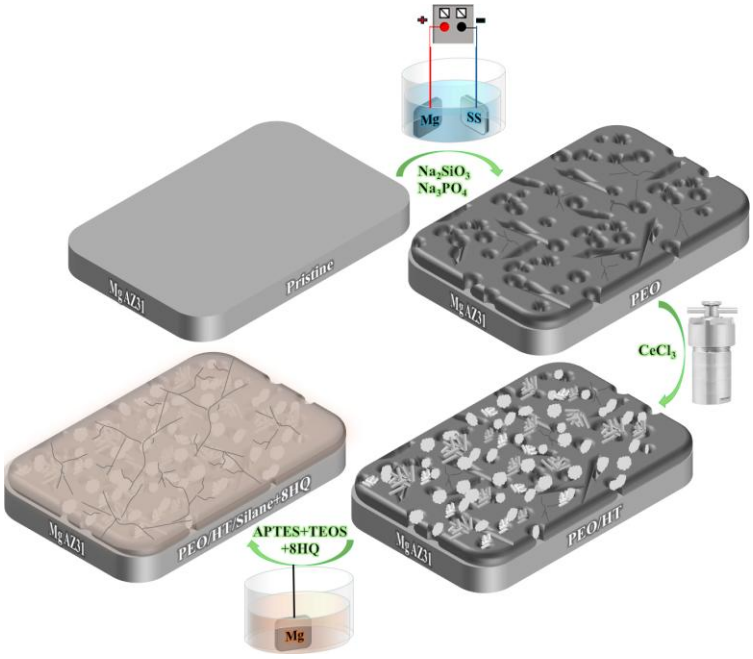


Figure 1: Schematic illustration of the preparation process of PEO/HT/Silane+8HQ composite coating.

2.3. Electrochemical Measurements

To investigate the effects of different coating systems on the corrosion characteristics of Mg-AZ31, Electrochemical Impedance Spectroscopy (EIS) was conducted using a BioLogic SP-200 electrochemical device. Impedance spectra were measured by applying a 10 mV AC signal over a frequency range of 100 kHz to 10 mHz at open circuit potential (OCP). A standard three-electrode glass cell was used, which incorporated an Ag/AgCl/saturated KCl reference electrode (0.197 V vs. SHE), a platinum foil as the auxiliary electrode, and coated samples as the working electrodes. The electrolyte used for characterization was 3.5% NaCl during 45 days. All experiments were carried out at laboratory temperature (~ 25 ºC). To calculate the standard deviation of the results and to assess their repeatability, all the corrosion tests were repeated three times. The impedance data were analyzed using Bode plots, which illustrate the logarithm of the impedance magnitude (|Z|) versus the logarithm of frequency (f), and the logarithm of frequency (f) against the phase angle (θ). The EIS spectra were then fitted using EC-Lab software.

2.4. Characterization

To assess the surface morphology, secondary electron microscopy (SEM; Quanta FEG 250, FEI) fitted with an EDX analyzer, FESEM Zeiss 55, were employed. The water contact angle was measured to investigate the wettability of different samples. Measurements were performed using a goniometer (model L2004A, Ossila) equipped with a digital camera. A distilled water droplet (~3 μL) was carefully deposited onto the sample surface at room temperature, and the droplet image was recorded after a few seconds of stabilization for further analysis. Time-of-flight secondary ion mass spectrometry (ToF-SIMS) measurements were conducted using a ToF-SIMS 4 system (IONTOF, Germany), which was equipped with a 25 keV Bi^+ liquid metal ion source, and X-ray photoelectron spectroscopy (XPS; SSX-100 S-probe, Surfaces Science Instruments, Mountain View, CA) with 200 W of Al Kα X-ray radiation (8.33 Å) was used to characterize the chemical composition of the surfaces, and the core level binding energies were calibrated using the reference C 1s peak located at 284.8 eV. The hydrogen evolution rate was determined using a gas chromatograph (SRI, Model 8610C, TCD detector) at 1, 3, 5, 8, 14, 24, 36, 55, and 80 h intervals [8,35].

3. Result and discussion

3.1. Microstructure

The morphology of PEO, PEO/HT, PEO/HT/Silane, PEO/HT/Silane+8HQ coatings (SEM) is presented in Figure 2a, b, c, and d respectively. Pores and cracks observed in the oxide structure of PEO coating in Figure 2a are mainly due to the application of high voltage, which leads to microchannel formation for electrical discharges [36], localized melting and solidification [37], gas evolution [38], and thermal stresses [39] during the oxidation reaction (Figure S1). The EDS results showed the presence of Mg, Al, and O with 36.12, 53.57, and 1.28 at%, respectively, as well as Si (6.41 at%) and P (2.62 at%) from the electrolyte. Figure 2b shows after HT treatment the

pores and cracks in the PEO layer are sealed with Ce salt (Ce^{+3}/Ce^{+4}) conversion coating and Ce containing particles (Figure S2). The EDS results showed that the coating is primarily composed of Ce, Mg, P, Si, and O elements.

Figure 2c and 2d show the silane layer with and without 8-HQ applied on the PEO/HT surface, covering the entire surface and providing improved sealing. It was observed that the silane coatings exhibited cracks. The addition of 8-HQ to the silane solution resulted in a higher number of cracks, but the coating covered the surface more uniformly (Figure S3). After the application of silane, hydrolysis and condensation take place between certain silanol and hydroxyl (OH) groups on the surface. Covalent Mg–O–Si bonds are created upon drying, establishing connections between the surface and the silane layer [40,41]. Hydrogen bonding also may occur between the amino group in APTES and the hydroxyl groups of the PEO coating [42]. TEOS, with its functional groups, can enhance the formation of Si–O–Si bonds [43]. The 8HQ not only has no adverse effect on the sol gel [44], but it has been shown to enhance the uniformity and density of the coating [45]. The EDS results indicate that the Si content increased with the addition of 8HQ.

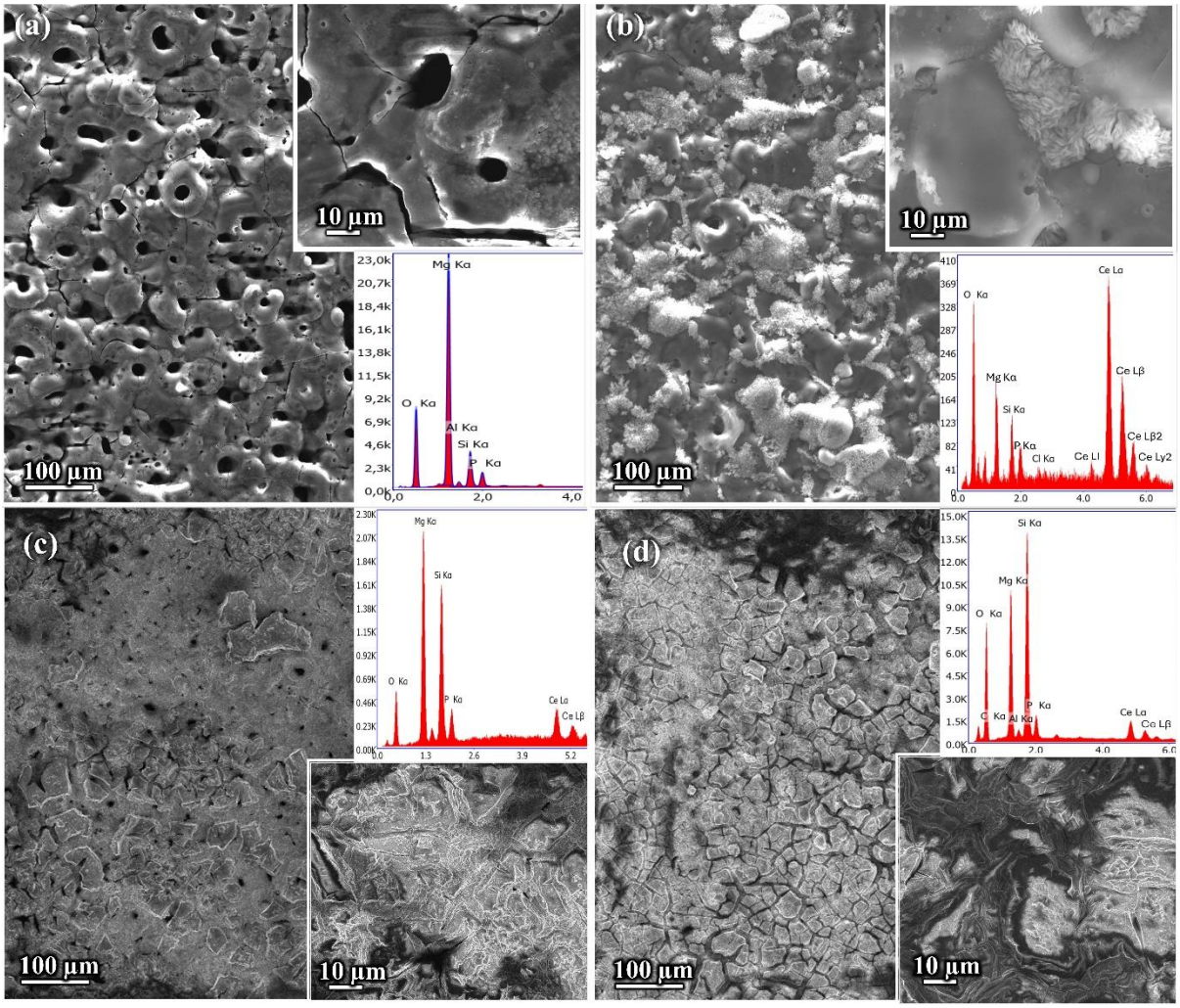


Figure 2: Surface morphologies of (a) PEO, (b) PEO/HT, (c) PEO/HT/Silane, and (d) PEO/HT/Silane+8HQ.

The cross-sectional images of the PEO coatings after the HT process, silane, and silane+8HQ applications are shown in Figure 3. The PEO, PEO/HT, PEO/HT/Silane, and PEO/HT/Silane+8HQ structures exhibited thickness values of 28.8 ± 11.6, 32.2 ± 3.3, 34.4 ± 4.3, and 33.7 ± 4.1 µm, respectively. Figure 3a shows the PEO coating is firmly bonded to the substrate. The layer closest to the Mg alloy matrix is relatively dense, while the outer part of the coating is more porous. Throughout the coating, there are holes and cracks of various sizes, which aligns with the characteristics shown in Figure 2a. After the hydrothermal treatment, the surface was covered by a thin layer of Ce, and the standard deviation of the thickness decreased due to the sealing of holes and cracks by Ce (Figure 3b). Applying silane

(Figure 3c) and silane+8HQ (Figure 3d) layers increased the coating thickness by approximately 2–3 µm. The silane layer enhanced surface sealing, and the silane+8HQ coating demonstrated a more uniform surface. The effective sealing ability of this type of silane coating precursor has also been reported in previous studies [13].

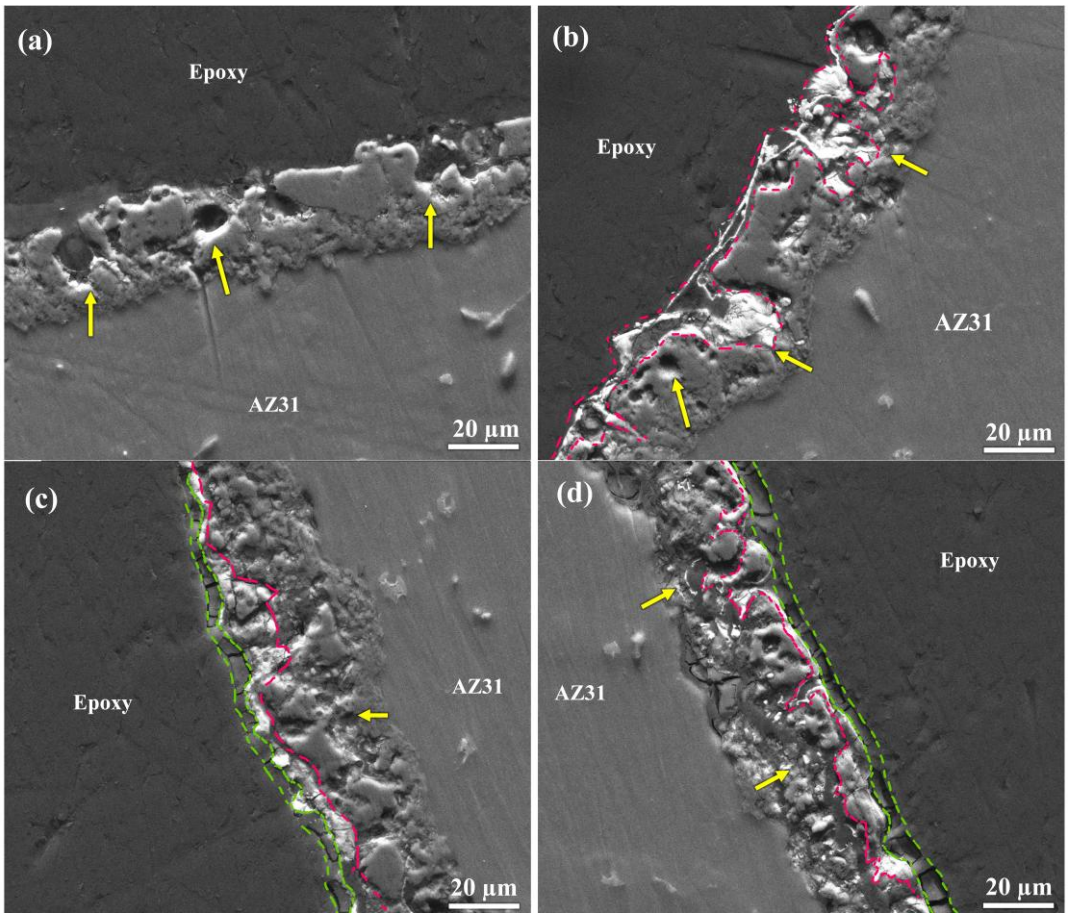


Figure 3: Cross-section morphologies of (a) PEO, (b) PEO/HT, (c) PEO/HT/Silane, and (d) PEO/HT/Silane+8HQ. Red line shows the Ce layer; green line shows the Silane layer.

Morphology and chemical composition of the PEO, HT, and silane layers can change the surface properties, which can be measured by static water contact angle investigation [46,47]. As shown in Figure S4, the uncoated AZ31 exhibits an average contact angle of ~20.6°. After PEO treatment, the contact angle increases (~67.7°) due to the formation of a porous oxide structure, followed by a slight increase after the HT process (~73.1°). In contrast, the silane layer decreases the contact angle to ~52.7°, while the addition of 8HQ leads to a slight increase

(~58.4°). The presence of terminal –NH_2 groups in the silane layer promotes hydrogen bonding with water molecules, resulting in increased wettability [48]. The surface free energy (γ_{sv}) and work of adhesion (W_a) were calculated using the Neumann [49] and Young [50] equations. Figure S5 shows that the PEO/HT sample has the lowest values of W_a and γ_{sv}, while the silane layer increases both parameters, indicating higher wettability.

XPS was used to identify the phases of the coatings following the sealing treatments, aiming to understand the principles behind the formation of various morphologies on different surfaces. Figure 4a presents XPS survey spectra for Ref (MgAZ31), PEO, PEO/HT, PEO/HT/Silane, and PEO/HT/Silane+8HQ. The results indicate that the PEO coating contains Si, which originates from the electrolyte composition. The shape of the spectra suggests that the majority of the oxide layer has formed as an amorphous structure [51]. After the HT process, the appearance of Ce 4d peaks indicates the presence of Ce in the composition, which was deposited and helped seal the pores and cracks in the PEO/HT sample. In the silane layer, the Si 2p peak corresponds to Si-O-Si bonds, and with the addition of 8HQ, an N 1s peak also appears. The high-resolution spectra of Si 2p for different samples in Figure 4b show that the Si-O-Si peak in the silane+8HQ sample is stronger than in the others. Although 8HQ does not contain Si, its functional groups can interact with the surface and modify its chemistry, which may promote the adsorption and condensation of silane precursors (APTES/TEOS), resulting in a stronger Si–O–Si signal [52]. In the PEO sample, the Si signal originates from the electrolyte composition, which disappears after the HT treatment. Therefore, the Si detected in the silane and silane+8HQ samples is attributed to the silane layer on the surface. The high-resolution XPS spectra of O 1s and Mg 2p in Figure 4c and f reveal that the O 1s signal is higher in the silane layers compared to others, due to the presence of both oxygen and silicon in their composition and the Mg 2p signal (substrate signal) decreases after the PEO coating. Figure 4d presents the deconvoluted high-resolution Ce 3d spectra for PEO/HT, PEO/HT/Silane, and

PEO/HT/Silane+8HQ samples, showing the characteristic Ce $3d_{5/2}$ and Ce $3d_{3/2}$ spin–orbit doublets and corresponding satellites. The spectra confirm the coexistence of both Ce^{3+} and Ce^{4+} oxidation states within the coating. Peaks at approximately 879.5 ± 1 eV and 886 eV correspond to the Ce^{3+} $3d_{5/2}$ component of the spin–orbit doublet, and those at 896 ± 1 eV and 906 ± 1 eV correspond to the Ce^{3+} $3d_{3/2}$ component. Ce^{4+} species are indicated by peaks at around 882.5 eV and 899 ± 1 eV for $3d_{5/2}$, and at 902.5 ± 1 eV and 915.5 ± 1 eV for $3d_{3/2}$, which are typical for Ce-based compounds. The atomic percentages of Ce calculated from XPS are 6.8% for PEO/HT, 2.1% for PEO/HT/Silane, and 1.0% for PEO/HT/Silane+8HQ, confirming the SEM observations in Figure 2. The addition of 8HQ led to a more uniform silane layer, covering the underlying layers more efficiently.

The deconvoluted high-resolution Si 2p spectra in Figure 4e display peaks at 100.1, 101.7, and 103.3 eV, corresponding to Si–O, silane (Si–O–Si), and fully oxidized SiO_2 states in the PEO/HT/Silane sample, respectively. In contrast, the Si 2p spectrum of the PEO/HT/Silane+8HQ sample shows peaks at 100.1 and 102.3 eV, attributed to Si–O and silane (Si–O–Si), respectively. The broader Si–O–Si peak and the absence of the fully oxidized SiO_2 signal can be attributed to the addition of HQ, which likely promotes the formation of other Si-based species such as Si–O–C and modified Si–O–Si structures. The atomic percentages of Si calculated from XPS are 4.9% for PEO/HT/Silane and 6.4% for PEO/HT/Silane+8HQ. The oxide composition formed during the PEO process may include Mg_2SiO_4 and $MgHPO_4$ [53] while in the PEO/HT coating, compounds such as CeO_2, Ce_2O_3, $Ce(OH)_4$, and $Ce(OH)_3$ can be present [32]. Figure 4g shows the high-resolution spectra of N 1s for the different coating systems. As shown, no N peak appears for the PEO/HT sample, while the N 1s signal is stronger in the PEO/HT/Silane+8HQ sample. This is attributed to the presence of N in the aromatic structure of 8HQ [54], in addition to the NH_2 group from the molecular structure of APTS [55]. The N 1s peak appears at 399.24 eV, while the N 1s peak corresponding to C–N=C bonds typically

appears at around 398.9 eV [56]. The positive shift in binding energy indicates that the chemical environment of N in the aromatic structure of 8HQ has changed after adsorption, confirming that chemical interaction occurred between the PEO/HT surface and the Silane+8HQ layer. The heat of adsorption of 8HQ on metallic surfaces is approximately 49.5 kJ/mol, which is sufficient to support a chemical reaction and confirms the occurrence of chemisorption on the metallic surfaces [57]. The chemisorption between Mg^{2+} and 8HQ leads to the formation of a stable $Mg(HQ)_2$ complex on the surface or within the coating structure [58].

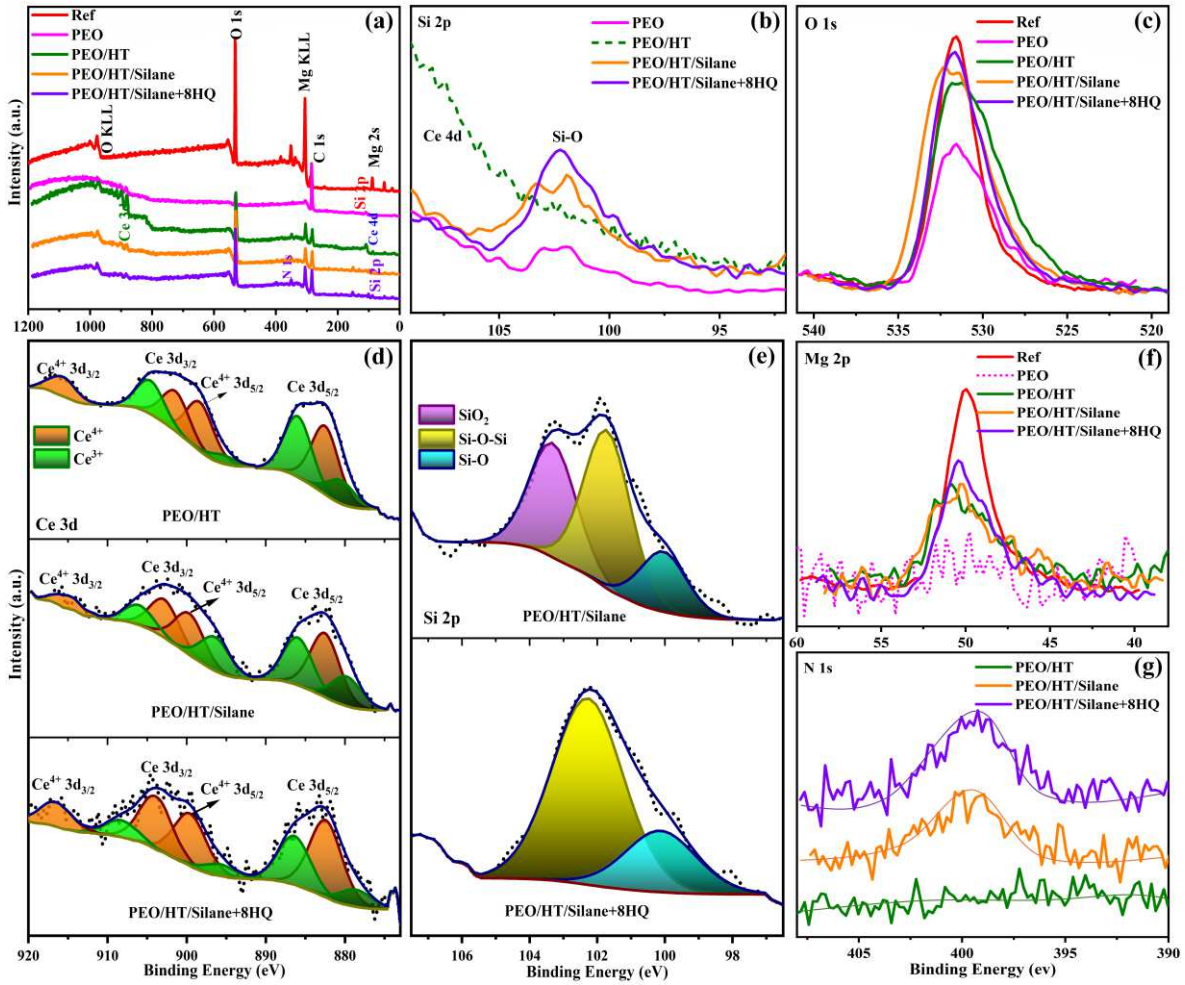


Figure 4: (a) XPS full survey spectra; high-resolution spectra of (b) Si 2p, (c) O 1s, and (d) Ce 3d for PEO/HT, PEO/HT/Silane, and PEO/HT/Silane+8HQ, (e) Si 2p for PEO/HT/Silane and PEO/HT/Silane+8HQ, (f) Mg 2p, and (g) N 1s for PEO/HT, PEO/HT/Silane, and PEO/HT/Silane+8HQ.

ToF-SIMS is widely used to investigate surface functionalization and confirm the presence of organic overlayers on oxide surfaces through characteristic molecular fragments [6]. To evaluate the distribution of surface species on Mg AZ31, ToF-SIMS combined with principal component analysis (PCA) was performed, with emphasis on verifying cerium incorporation and the formation of a hybrid silane-8-hydroxyquinoline layer on the PEO coating. The positive ion spectra for the Ref (MgAZ31), PEO/HT, and PEO/HT/Silane+8HQ samples are presented in Figure 5a-c. The Mg^+ fragment exhibits the highest intensity for the reference sample (Figure 5a). In contrast, a significant decrease is observed for the coated samples, indicating effective surface coverage of the Mg AZ31 substrate. As shown in Figure S6 a, the Mg^+ signal is higher for the PEO/HT coating than for the PEO/HT/silane+8HQ sample, further confirming a reduction of the substrate signal after formation of the hybrid overlayer.

The PEO/HT coating is characterized by strong cerium-related fragments, with a prominent signal at m/z 155.9 corresponding to CeO^+ in Figure 5b, confirming the presence of Ce-based sealing species. Since ToF-SIMS is a surface-sensitive technique, the lower CeO^+ intensity observed in the hybrid coating indicates a decrease in the cerium signal due to the formation of an overlying hybrid silane-organic layer. In contrast, the PEO/HT/Silane+8HQ sample shows fragments associated with silane and organic species, including Si-containing fragments at m/z 73 ($SiC_2H_5O^+$, Figure 5c) and nitrogen-containing ions shown in Figure S4, such as m/z 59 ($C_2H_5NO^+$), m/z 147 ($C_9H_9NO^+$/ $SiC_5H_{13}NO_2^+$), and m/z 207 ($SiO_2C_9H_9NO^+$), confirming the presence of both silane-derived species and 8-hydroxyquinoline-related fragments within the hybrid matrix. The PCA score plot (Figure 5d) shows a clear separation between the PEO/HT and PEO/HT/silane+8HQ samples, indicating differences in their surface chemistry. The loading plot in Figure 5e supports this separation, which highlights the mass fragments responsible for distinguishing the two sample groups. The corresponding fragment assignments are summarized in Table S 1. The observed differences indicate that incorporation of silane and

8-hydroxyquinoline modifies the surface chemistry of the coating. The PEO/HT sample is mainly characterized by cerium-related fragments, while the hybrid coating exhibits a higher contribution from silicon- and nitrogen-containing species. To evaluate these changes, two fragment ratios were used as semi-quantitative surface chemical indices. The $SiC_2H_5O^+/CeO^+$ ratio (1.08 ± 0.53 for PEO/HT and 362.35 ± 3.00 for PEO/HT/silane+8HQ) reflects the relative surface abundance of silane species compared to cerium-related signals, where higher values indicate an increased contribution of the silane network at the outer surface. The $C_2H_5NO^+/CeO^+$ ratio (0.083 ± 0.032 for PEO/HT and 74.32 ± 4.06 for PEO/HT/silane+8HQ) represents the relative surface contribution of nitrogen-containing organic species associated with APTES and 8-hydroxyquinoline. The higher ratios for the PEO/HT/silane+8HQ coating indicate the formation of a silane-8HQ-enriched surface layer, which modifies the outermost surface chemistry and results in a lower relative contribution of cerium-related signals.

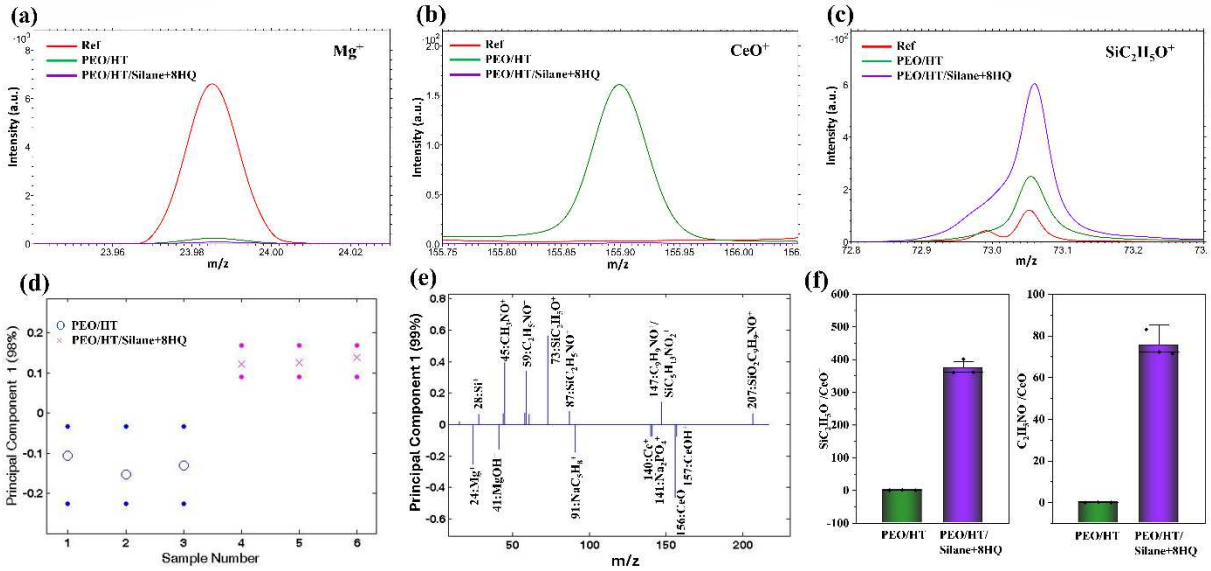


Figure 5: (a-c) Positive ToF-SIMS ion images of molecular fragments: (a) Mg^+, (b) CeO^+, and (c) $SiC_2H_5O^+$ for Ref (Mg AZ31), PEO/HT, and PEO/HT/silane+8HQ samples. (d-e) PCA analysis of ToF-SIMS data for PEO/HT and PEO/HT/silane+8HQ samples: (d) score plot of positive ion spectra and (e) corresponding loading plot, where signals are labeled with their mass-to-charge ratios and assigned fragments. The dotted lines in the score plot represent the 95% confidence limits. (f) ToF-SIMS peak intensity ratios used as semi-quantitative surface chemical indices for PEO/HT and

PEO/HT/silane+8HQ samples. All ratios were normalized to total ion intensity, and error bars represent standard deviations (n = 3).

3.2. Corrosion Behavior

To evaluate the effectiveness of various coating systems, a 45-day EIS test was performed in a 3.5% NaCl corrosive solution. Nyquist, Bode modulus, and Bode phase plots for the PEO single-layer, PEO/HT, PEO/HT/Silane, and PEO/HT/Silane+8HQ coated samples are shown at different immersion times (1-1100 h) in Figure 6, Figure 7, Figure 8, and Figure 9. The Nyquist plots display semi-elliptical arcs, indicating a standard passive state characterized by high impedance values and a capacitive response. The asymmetric shape of these semicircles indicates a frequency dispersion attributed to physical phenomena such as surface roughness due to PEO structure, and the distribution of surface-active sites, for which constant phase elements (CPE) are preferably used instead of ideal capacitors in the equivalent circuit models of the electrodes to fit the experimental data [8]. Therefore, equivalent circuits (EC) considered with Q as a CPE where a capacitor usually exists between each interface to compensate for system inhomogeneity caused by the rough or porous surface of the sample, with two time constants in the presence or absence of the inductor, were employed to fit the EIS data, as shown in Figure 10. Rs refers to the uncompensated solution resistance, which is the impedance between the counter electrode and the working electrode. Qc and Rc at higher frequencies, representing the coating CPE and coating resistance, respectively. Similarly, Qdl and Rct correspond to the electron double-layer capacitance and charge transfer resistance of the Mg substrate at the bottom of the PEO coating. The resistance and capacitance associated with the dense inner layer of the PEO coating are reflected in the Rct and Qdl values [59]. RL represents the resistance to localized corrosion, which includes inductance (L). In addition, the data obtained from fitting the impedance spectra using the appropriate EC is presented in Table 1.

Figure 6a, b, c shows the Nyquist and Bode diagrams of samples after 1, 8, and 24 h immersion in 3.5% NaCl solution at OCP and room temperature, respectively. According to the results, the Ref sample exhibits inductive behavior, which is often attributed to the adsorption of chloride ions (Cl^-), initiating localized corrosion, such as pitting. Additionally, it may be related to the high concentration of Mg ions in relatively film-free areas, or intermediate steps in the corrosion process involving adsorbed species on the surface, such as $Mg(OH)^+$, $Mg(OH)_2$, and Mg^{2+}. These species reflect dynamic surface reactions that contribute to the overall corrosion mechanism [60]. The corrosion resistance of the PEO sample remained almost stable after 24 h. While the PEO/HT and PEO/HT/Silane coatings showed similar performance at the initial immersion times, the PEO/HT/Silane coating exhibited improved corrosion resistance after 24 h. Notably, the PEO/HT/Silane+8HQ coating demonstrated superior corrosion resistance throughout the entire immersion times.

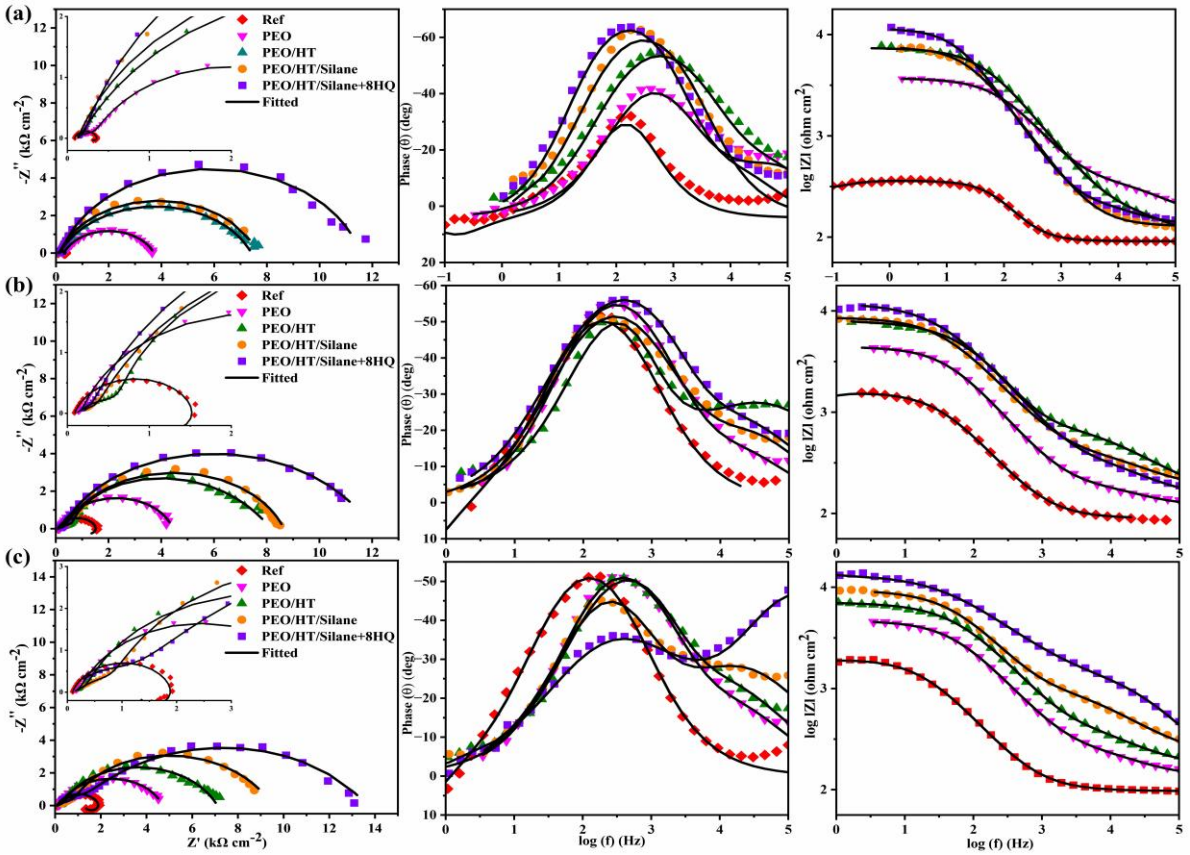


Figure 6: Nyquist and Bode plots of Ref, PEO, PEO/HT, PEO/HT/Silane, and PEO/HT/Silane+8HQ after (a) 1, (b) 8, and (c) 24 h immersion in 3.5% NaCl solution at room temperature.

Figure 7a, b, c shows the EIS results after 72, 168, and 264 h, respectively. An increase in impedance values, along with low phase angle dispersion at low frequencies, is observed and is typically associated with reduced corrosion of all the samples. For the Ref sample, the inductive loop disappears after 168 hours, likely due to the formation of a $Mg(OH)_2$ or MgO layer on the surface, which disrupts charge transfer at the Mg/electrolyte interface. Similar layers can also form more adherently on the PEO sample due to the composition of the PEO layer, which contains silicate and phosphate species (Figure 2a). These compounds contribute to sealing the pores and cracks in the PEO coating, thereby enhancing its barrier properties. For the PEO/HT, PEO/HT/Silane, and PEO/HT/Silane+8HQ coatings, this effect is more pronounced due to the additional sealing by Ce-based hydrothermal treatment and silane layers, with or without 8HQ. This explains why their corrosion resistance remained significantly higher over time, as the sealing treatments effectively prevent the penetration of corrosive species such as Cl^- ions, oxygen molecules, and water into the PEO coating, primarily through its pores, which otherwise act as diffusion pathways for these agents [61].

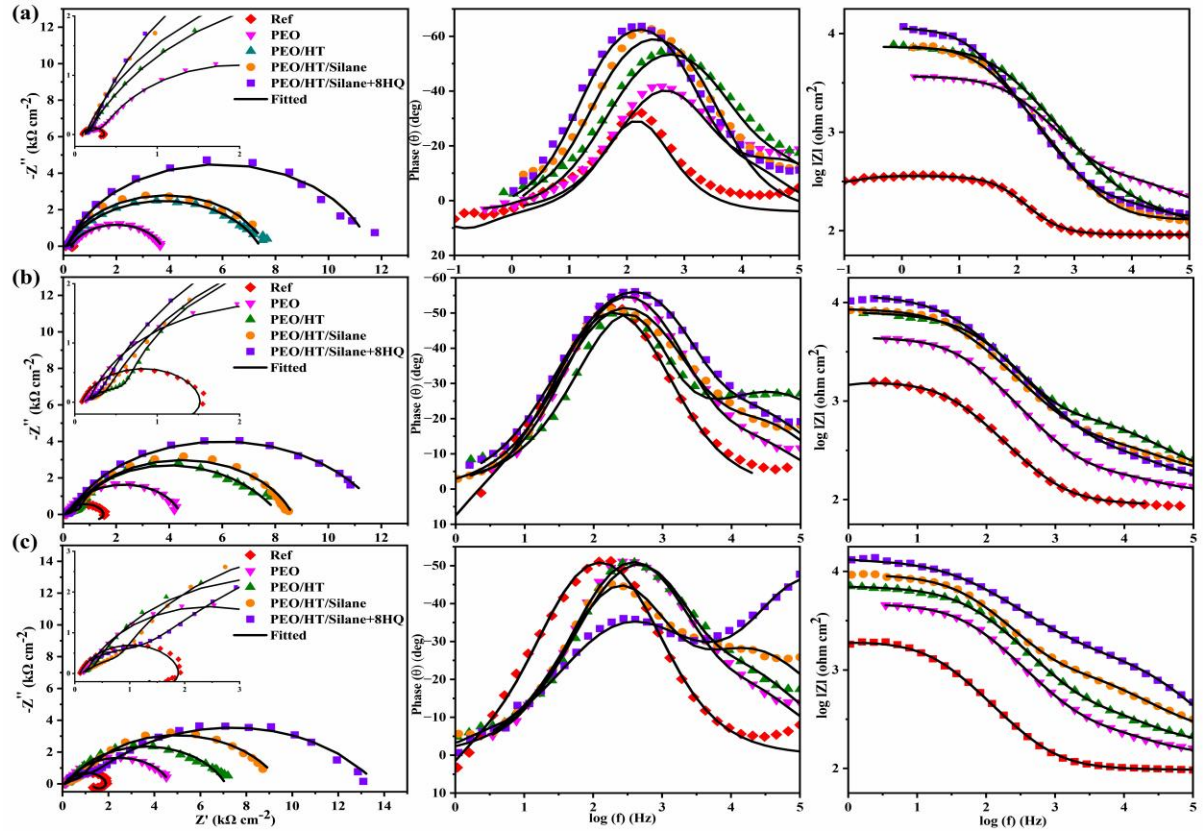


Figure 7: Nyquist and Bode plates of Ref, PEO, PEO/HT, PEO/HT/Silane, and PEO/HT/Silane+8HQ after (a) 72, (b) 168, and (c) 264 h immersion in 3.5% NaCl solution at room temperature.

An interesting phenomenon was observed for the PEO/HT, PEO/HT/Silane, and PEO/HT/Silane+8HQ samples after 168 and 264 h (Figure 7b and c), and at 384 h (Figure 8a) immersion in 3.5% NaCl. Their electrochemical behavior changed noticeably, as indicated by the emergence of a second time constant in the EIS results. This transition was accompanied by a notable increase in impedance and a decrease in phase angle, particularly for the PEO/HT/Silane+8HQ sample. In addition, the phase angle in the intermediate frequency range becomes broader, while the phase angles at low and high frequencies become less distinct. Therefore, it can be concluded that the inhibitory effects of Ce and chelating capabilities of 8HQ were activated, helping the coatings maintain good corrosion resistance during long-term exposure to the corrosive solution, whereas the impedance of the PEO sample began to decline after 264 h of immersion [62,63].

Figure 8b shows that after 432 h of immersion, the coatings appear to lose their protective effectiveness due to the penetration of corrosive ions, leading to a sharp drop in impedance for all coated samples. This decreasing trend continued after 600 h, as shown in Figure 8c. Ce and 8HQ no longer revealed considerable inhibitory effects, likely due to their gradual consumption with prolonged exposure to the corrosive 3.5% NaCl. Figure 9a and b also depict the results after 840 and 1100 h, respectively, where an inductive loop reappeared in the PEO sample, indicating that it had lost its protective functionality.

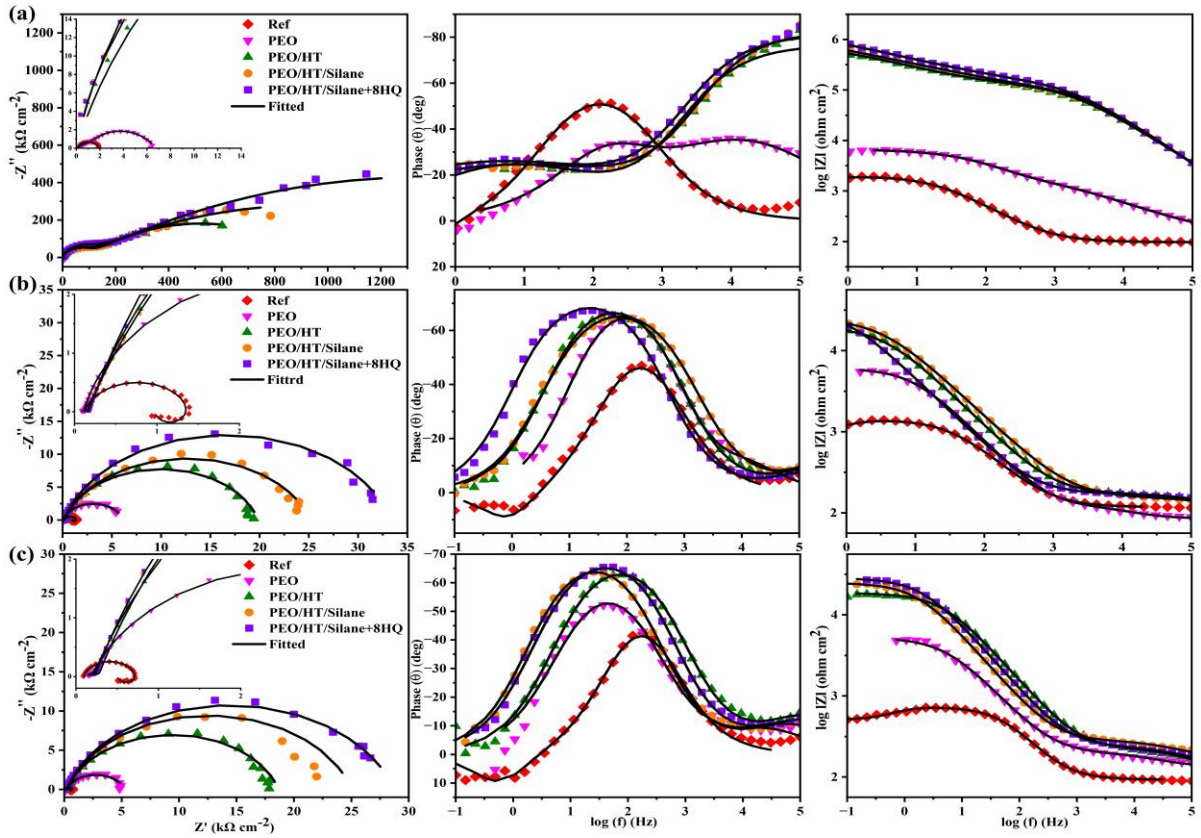


Figure 8: Nyquist and Bode plates of Ref, PEO, PEO/HT, PEO/HT/Silane, and PEO/HT/Silane+8HQ after (a) 384, (b) 432, and (c) 600 h immersion in 3.5% NaCl solution at room temperature.

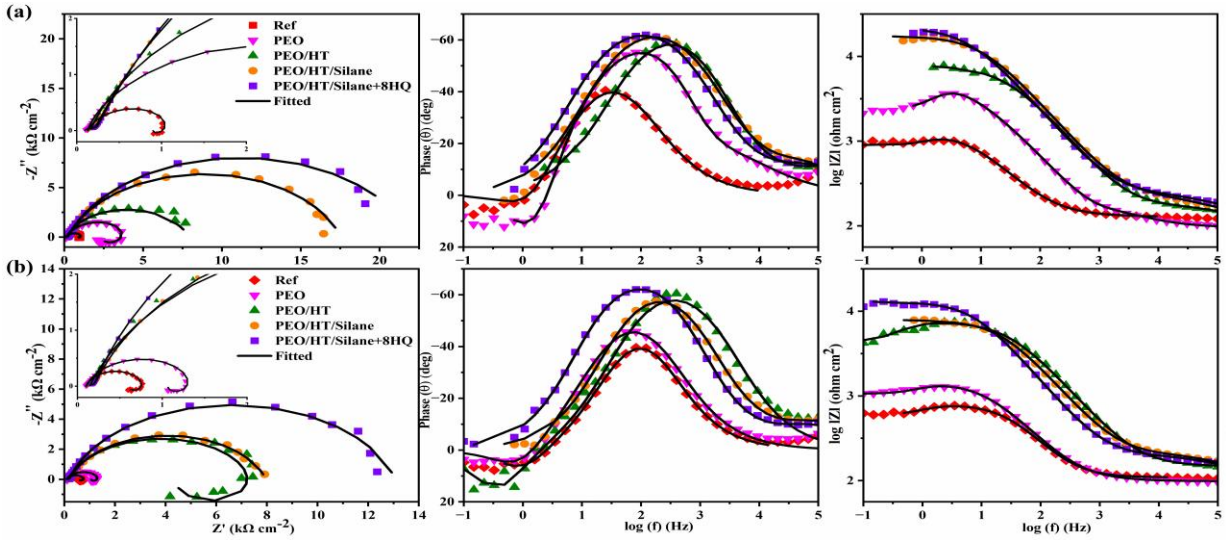


Figure 9: Nyquist and Bode plates of Ref, PEO, PEO/HT, PEO/HT/Silane, and PEO/HT/Silane+8HQ after (a) 840, and (b) 1100 h immersion in 3.5% NaCl solution at room temperature.

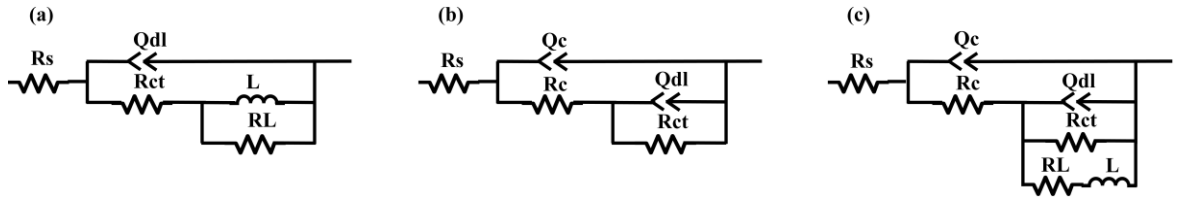


Figure 10: Equivalent circuit models for EIS fitting (a) untreated (b) and (c) coated samples.

Table 1 and Figure 11 present the corrosion resistance, represented by the total faradic resistance R_T (R_{ct}+R_c), for each sample at different immersion times, as calculated from the fitted EIS data. The overall faradaic resistance correlates with the diameter of the depressed capacitive semicircle seen in the Nyquist plots. After 24 h of immersion, the Rt of the Ref sample increased from 0.21 to 1.20 kΩ.cm^2 (compared to 1 h), then fluctuated between 0.4–0.9 kΩ.cm^2, indicating a progressive corrosion rate and the formation of unstable corrosion products on the surface. The PEO sample exhibited an R_T of 3.61 kΩ.cm^2 after 1 h of immersion, which increased to 24.55 kΩ·cm^2 at 168 h due to the formation of Si- and P-rich corrosion products that temporarily acted as a barrier to corrosive ion penetration, but after 264 h the R_T dropped sharply to 8.81 kΩ.cm^2 as aggressive ions diffused through pores and cracks in the PEO layer, destabilizing the barrier, and by 840 h inductive behavior was observed, leading the onset of localized corrosion on the surface (see Figure 13).

Table 1: Fitted parameters for EIS spectrum depicted in Figures 5-8.

Sample	Time (h)	R_s [Ω cm^2]	Rc [k.Ω cm^2]	Qc [S s^n cm^{-2}]	n	Rct [k.Ω cm^2]	Q_{ct} [S s^n cm^{-2}]	n	R_L [Ω cm^2]	L [H]	χ^2	R_T [k.Ω cm^2]
Ref	1	91.03				0.21	1.62E-5	0.89	65.98	57.12	0.03	0.21
	8	89.23				0.88	7.99E-6	0.82	612.30	177.60	0.02	0.88
	24	96.84				1.20	1.03E-5	0.81	666.30	325.60	0.06	1.20
	72	89.88				0.92	8.89E-6	0.83	242.30	28.00	0.01	0.92
	168					0.83	9.36E-6	0.94	151.20	138.9	0.03	0.83
	264	90.91				0.45	1.24E-5	0.91	233.60	125.50	0.04	0.45
	384	86.13				0.55	9.84E-6	0.81	293.70	70.39	0.02	0.55
	432	98.20				0.86	7.81E-6	0.83	437.60	66.27	0.02	0.86
	600	92.67				0.42	1.11E-5	0.85	220.30	49.47	0.02	0.42
	840	99.30				0.78	4.37E-5	0.77	366.60	35.59	0.01	0.78
	1100	96.72				0.49	1.81E-5	0.83	201.60	26.99	0.003	0.49
PEO	1	105.37	0.29	5.96E-7	0.72	3.31	1.64E-6	0.78			0.02	3.61
	8	99.71	0.12	6.68E-7	0.83	4.22	1.54E-6	0.83			0.01	4.34
	24	107.30	0.20	7.72E-7	0.79	4.34	1.27E-6	0.81			0.01	4.59
	72	117.90	0.75	5.26E-6	0.54	14.54	3.61E-7	0.85			0.01	15.28
	168	113.94	2.04	3.49E-6	0.49	22.51	1.17E-6	0.77			0.01	24.55
	264	107.10	0.77	2.25E-7	0.81	8.04	2.39E-6	0.80			0.02	8.81
	384	123.00	2.26	2.41E-6	0.59	4.43	9.14E-7	0.83			0.01	6.67
	432	94.33	0.56	1.75E-6	0.81	5.46	2.83E-6	0.89			0.02	6.01
	600	130.60	0.58	1.87E-6	0.75	4.59	9.47E-6	0.80			0.09	5.17
	840	94.90	0.15	1.29E-6	0.68	4.79	7.73E-7	0.98	1.91	538.60	0.01	4.94
	1100	93.21	0.22	6.04E-6	0.79	1.10	1.38E-5	0.81	1.79	789.56	0.02	1.32
PEO/ HT	1	101.04	0.12	3.87E-7	0.80	7.18	1.43E-6	0.75			0.03	7.31
	8	118.70	0.85	2.13E-6	0.59	7.22	2.31E-7	0.97			0.03	8.07
	24	167.24	0.47	1.48E-6	0.69	6.47	3.59E-7	0.87			0.04	6.94
	72	114.40	0.42	2.39E-6	0.61	11.38	6.14E-7	0.88			0.04	11.79
	168	189.67	10.41	2.2E-8	0.77	58.15	2.89E-6	0.50			0.007	68.56
	264	201.98	68.24	2.05E-8	0.73	388.95	1.05E-6	0.48			0.07	457.19
	384	289.25	114.95	3.16E-9	0.85	822.28	5.13E-7	0.52			0.07	937.23
	432	118.30	0.56	1.99E-7	0.84	19.13	3.38E-6	0.83			0.02	19.69
	600	112.70	0.12	5.32E-7	0.74	18.44	2.75E-6	0.83			0.01	18.57
	840	89.02	0.20	1.63E-6	0.63	7.68	1.16E-6	0.85			0.08	7.88
	1100	146.50	4.25	1.93E-6	0.80	3.17	1.32E-11	0.69	1.31	1003	0.09	7.41
PEO/ HT/ Silane	1	109.30	0.11	8.58E-7	0.81	7.12	9.21E-7	0.86			0.03	7.23
	8	180.70	0.27	4.48E-7	0.77	8.12	1.19E-6	0.79			0.04	8.47
	24	193.20	1.10	1.22E-6	0.64	8.24	4.89E-7	0.86			0.03	9.34
	72	133.30	0.28	3.08E-7	0.73	28.98	1.85E-6	0.79			0.02	29.26
	168	98.25	10.49	2.44E-8	0.77	59.46	2.17E-6	0.57			0.01	69.95
	264	114.01	69.79	1.34E-8	0.76	284.12	8.10E-7	0.46			0.07	353.99
	384	255.10	82.57	1.35E-9	0.91	663.89	6.56E-7	0.40			0.02	746.46
	432	84.32	0.57	1.27E-7	0.80	24.49	3.20E-6	0.81			0.01	25.06
	600	162.50	0.63	8.95E-7	0.72	24.24	4.72E-6	0.84			0.02	24.87
	840	139.00	0.31	3.58E-7	0.81	17.10	1.58E-6	0.80			0.03	17.41
	1100	129.80	0.59	3.37E-7	0.80	7.25	1.97E-6	0.82			0.01	7.83
PEO/ HT/ Silane +8HQ	1	135.10	0.62	6.10E-7	0.85	10.77	1.20E-6	0.85			0.03	11.39
	8	137.70	0.38	1.49	0.69	11.50	3.27E-7	0.87			0.01	11.87
	24	83.74	1.36	6.70E-8	0.77	12.21	1.855E-6	0.64			0.02	13.57
	72	63.79	0.28	2.09E-7	0.72	42.36	2.31E-6	0.73			0.03	42.64
	168	321.25	8.78	1.85E-8	0.79	77.38	3.13E-6	0.48			0.01	86.15
	264	201.89	82.21	2.10E-9	0.89	412.16	1.10E-6	0.28			0.01	494.37
	384	398.29	115.15	1.66E-9	0.90	1,087.5	5.17E-6	0.42			0.04	1,202.6
	432	127.80	0.54	1.13E-7	0.91	32.59	6.36E-6	0.84			0.03	33.14
	600	124.30	0.62	1.01E-6	0.69	28.00	3.27E-6	0.84			0.03	28.63
	840	147.9	0.61	3.91E-7	0.79	21.36	2.00E-6	0.80			0.01	21.97
	1100	130.30	0.58	4.49E-7	0.80	12.36	2.65E-6	0.83			0.01	12.94

The standard deviation range for Rs, Rc, Rct, and R_L values is between 2.8% and 4.9%.
The standard deviation range for Qc, Qdl, values is between 1.7% and 4.5%.

After 384 h of immersion the R_T values were 937.23 and 746.46 kΩ.cm^2 for the PEO/HT and PEO/HT/Silane samples, respectively. Although the PEO/HT sample showed the higher value, the PEO/HT/Silane sample exhibited a better average protective performance throughout the 1100 h immersion period. This can be attributed to the controlled release kinetics of Ce^{+3}/Ce^{+4} ions, which can be further modulated by applying a secondary coating layer [32]. By adding 8HQ to the silane coating, the R_T increases significantly from 11.39 to 1200 kΩ.cm^2 over the 1 to 384 h period, and then decreases to 12.94 kΩ.cm^2 after 1100 hours. The PEO/HT/Silane+8HQ system demonstrates superior corrosion resistance after 16 days of immersion in 3.5% NaCl. This improvement can be due to the formation of an additional protective layer on the Mg surface, containing 8HQ(Mg) formation, which leads to a significant increase in impedance modulus in the high-frequency range [64].

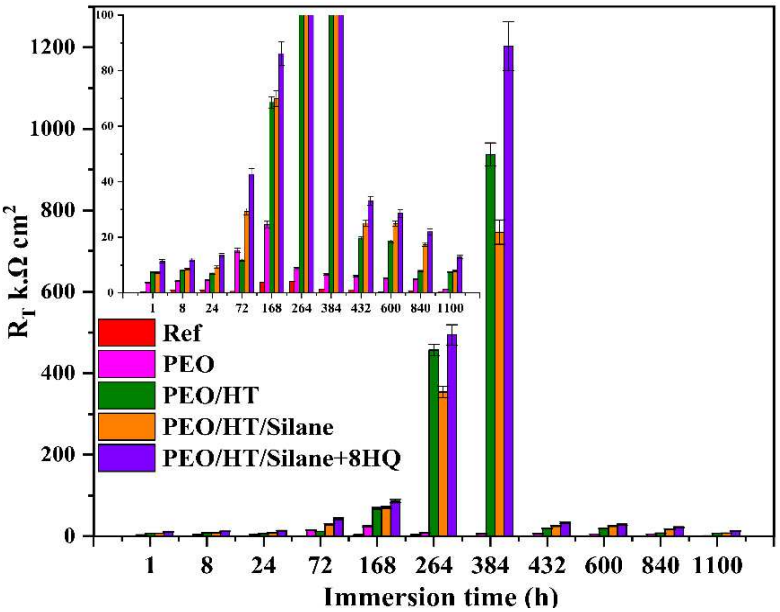


Figure 11: total faradic resistance RT (Rct+Rc) of different samples at various immersion times. Inset shows a higher magnification of lower signals.

Figure 12 shows the H_2 evolution rates of different coating systems after 30 days of immersion in 3.5% NaCl, measured over 80 h. In the case of Mg in aqueous solutions, the primary anodic reaction (Eq. 1) accompanied with cathodic reaction (Eq. 2) is typically the reduction of water, since H_2 evolution dominates due to the low standard electrode potential of Mg.

$$Mg \rightarrow Mg^{2+}+2e^{-} \quad (1)$$

$$2H_2O+2e^{-} \rightarrow H_2 \uparrow +2OH^{-} \quad (2)$$

This reaction represents the hydrogen evolution reaction (HER), which occurs during corrosion of Mg in neutral or alkaline aqueous environments [8]. The uncoated sample consistently exhibits the highest corrosion rate, while the PEO/HT/Silane+8HQ coating shows significantly lower corrosion compared to the other samples. The H_2 evolution rates for Ref, PEO, PEO/HT, PEO/HT/Silane, and PEO/HT/Silane+8HQ were 270±26, 174±15, 80±12, 65±14, and 38±9 µL cm^{-2}, respectively. The H_2 evolution results corroborate the EIS findings, demonstrating that Ce and 8HQ provide excellent synergistic inhibitory performance, which significantly enhances corrosion protection.

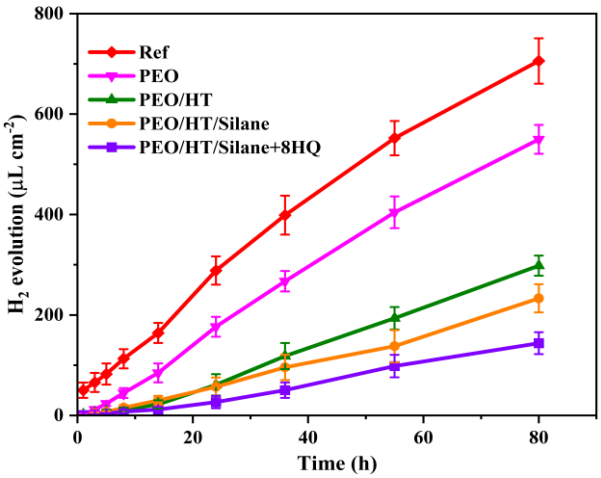


Figure 12: H_2 evolution rates for Ref, PEO, PEO/HT, PEO/HT/Silane, and PEO/HT/Silane+8HQ after 30 days of immersion in 3.5% NaCl, measured at 1, 3, 5, 8, 14, 24, 36, 55, and 80 h intervals.

Figure 13 presents the surface morphologies (Photographs) of the Ref, PEO, PEO/HT, PEO/HT/Silane, and PEO/HT/Silane+8HQ samples at various immersion times. It is evident that a portion of the PEO coating delaminated from the surface after 264 h of immersion due to corrosion. In contrast, the sealed samples, particularly PEO/HT/Silane+8HQ remained intact with no visible signs of corrosion up to this point. Corrosion signs began to appear after 432 h, which corresponded with a sharp decrease in impedance.

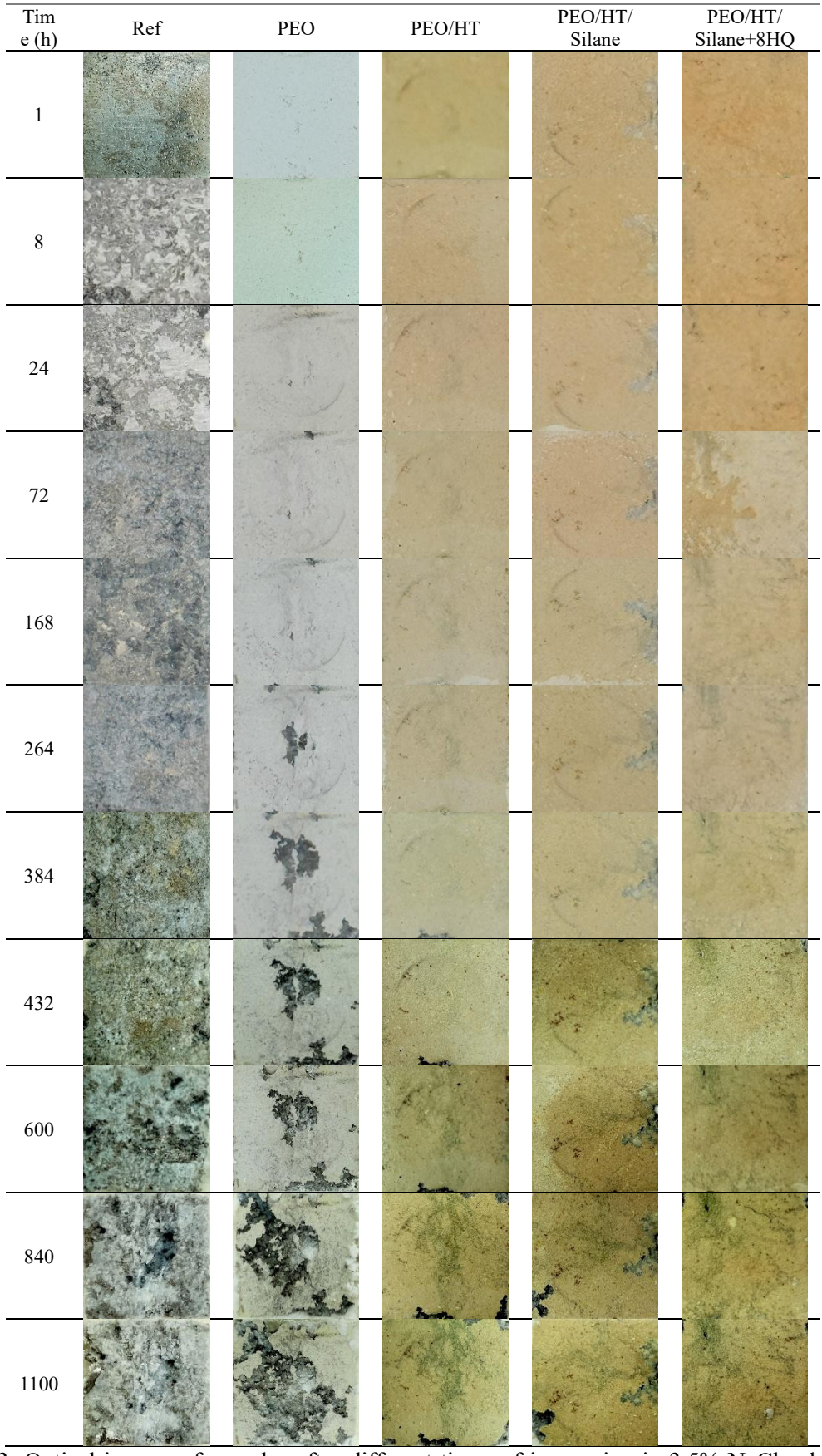


Figure 13: Optical images of samples after different times of immersion in 3.5% NaCl solution. (all squares have a side length ≈10 mm).

After 1100 h of immersion, the PEO/HT/Silane+8HQ coating remained well adhered to the surface without serious degradation. In contrast, the Ref and PEO samples exhibited severe localized (pitting) corrosion, whereas the sealed samples showed only minor pitting or localized corrosion in isolated areas. Based on the results discussed above, a possible corrosion protection mechanism is proposed to explain the excellent corrosion resistance of the hybrid coating. Figure 15 schematically illustrates the corrosion and inhibition mechanisms of the different samples in NaCl solution. On one hand, the PEO coating with high porosity is sealed with Ce based particles trough the HT reaction in the Ce salt solution. The silane layer forms strong Mg–O–Si/Ce bonds with the PEO surface through hydrolysis and condensation reactions, while unreacted silanol groups create a dense Si–O–Si network [43]. Functional groups in TEOS and APTES enhance bonding and enable control over Ce release, improving long-term corrosion resistance. As confirmed by XPS results, indicating the presence of Ce^{3+} and Ce^{4+} on the surface, Ce ions are gradually released during the corrosion process and react with OH^- ions [65]. These Ce ions outcompete other cations such as Mg^{2+} to form insoluble precipitates, which accumulate at active sites, plugging cracks and pores [14,65]. By adding 8HQ into the silane layer, the inhibitory effect of 8HQ on Mg alloys is notably enhanced, thereby improving the protective performance. As illustrated in Figure 14, 8HQ can form a highly insoluble Mg-chelate complex ($Mg(HQ)_2$) at anodic sites [58,64]. This effect, combined with the Ce-containing product layer, results in a synergistic mechanism that merges the physical barrier of the coating with the formation of a dense, protective layer.

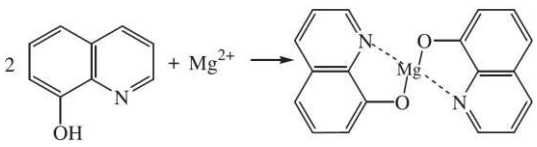


Figure 14: The complexation of 8HQ with Mg, forming a highly insoluble Mg-chelate complex.

As corrosion of the substrate progresses, corrosion products begin to accumulate at the PEO/substrate interface, increasing mechanical stress on the upper layers. Simultaneously, Ce ions and 8HQ are locally consumed through the formation of Ce-containing precipitates and $Mg(8HQ)_2$ complexes. By extending time, the accumulation of corrosion products and the generation of hydrogen bubbles induce pitting and cracking in the protective top layer, allowing greater diffusion of aggressive Cl^- ions toward the substrate. This deterioration is evidenced by the sharp decline in impedance values after 18 days (432 h) of immersion.

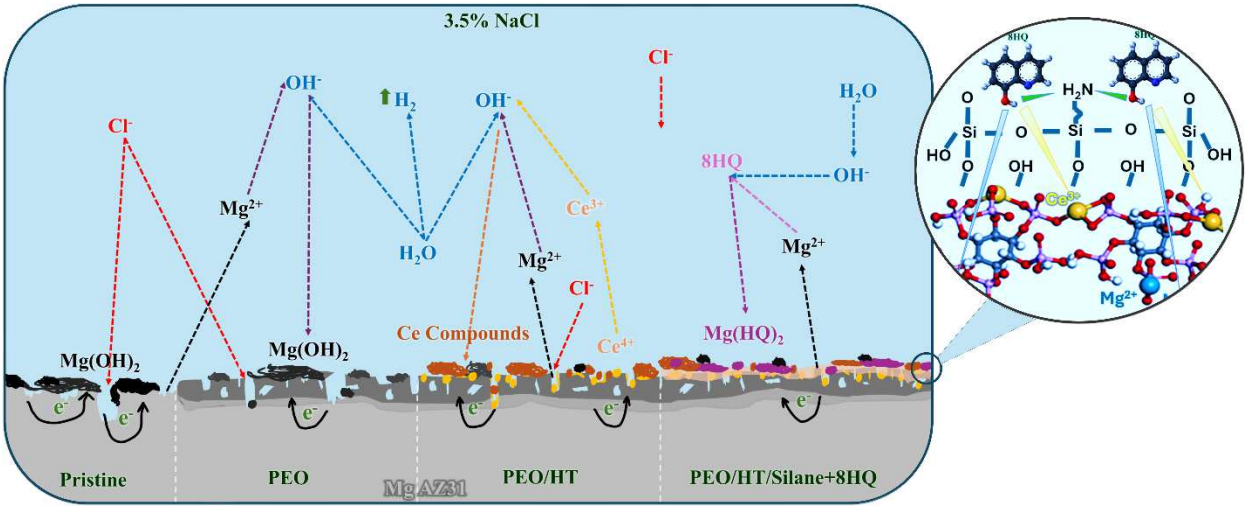


Figure 15: Schematic illustration of the corrosion protection mechanisms provided by Ce and 8HQ in the PEO/HT and PEO/HT/Silane+8HQ coatings, in comparison with the Ref and PEO samples.

4. Conclusion

In this study a hydride PEO/HT/Silane+8HQ coating with long term corrosion resistance successfully prepared on Mg AZ31 alloy through combining PEO, hydrothermal and sol-gel methods. Its anti-corrosion nature is derived from not only the innate physical barrier but also the additional anti-corrosion behavior of Ce and 8HQ synergistically. The Ce on the surface of the coating are continuously dissolved to fill the cracks, so that the coating can still maintain high corrosion resistance in the case of long-time immersion. The addition of 8HQ further improved protection by forming insoluble chelates and contributing to the formation of a dense

silane layer. EIS results confirmed active corrosion inhibition, with the present of Ce–8HQ showing up to a 100-fold improvement in resistance. Surface analyses revealed early delamination in unsealed coatings, while PEO/HT/Silane+8HQ remained largely intact up to 432 h. H_2 evolution tests supported these findings, showing the lowest gas release (38 ± 9 µL cm^{-2}) for the PEO/HT/Silane+8HQ coating after 30 days, highlighting its superior long-term performance.

Acknowledgments

This work was conducted at the University of Siegen within the Chemistry & Structure of novel Materials (CSnM) research group. The authors thank the DFG (KI 2169/2-1) and the European Union (EU-RIA NOMAD, 101091669) for funding this work. The Micro and Nanoanalytics Facility (MNaF), funded by the DFG (DFG INST 221/131-1), at the University of Siegen.

References

1. Atrens, A. *et al.* Review of recent developments in the field of magnesium corrosion. *Adv. Eng. Mater.* **17**, 400–453 (2015).
2. Abbott, T. B. Magnesium: Industrial and Research Developments Over the Last 15 Years. *Corrosion* **71**, 120–127 (2015).
3. Cao, F., Song, G. L. & Atrens, A. Corrosion and passivation of magnesium alloys. *Corros. Sci.* **111**, 835–845 (2016).
4. Aparicio, M. *et al.* Self-Healing Engineered Multilayer Coatings for Corrosion Protection of Magnesium Alloy AZ31B. *ACS Materials Au* **5**, 420 (2025).
5. Khan, M. A., Safira, A. R., Kaseem, M. & Fattah-alhosseini, A. Enhanced electrochemical and photocatalytic performance achieved through dual incorporation of SnO2 and WO3 nanoparticles into LDH layer fabricated on PEO-coated AZ31 Mg alloy. *Journal of Magnesium and Alloys* **12**, 1880–1898 (2024).
6. Killian, M. S., Wagener, V., Schmuki, P. & Virtanen, S. Functionalization of metallic magnesium with protein layers via linker molecules. *Langmuir* **26**, 12044–12048 (2010).
7. Lu, X. *et al.* Comprehensive study on corrosion, wear and fatigue performance of low-porosity PEO coating on Mg alloy. *Journal of Magnesium and Alloys* https://doi.org/10.1016/J.JMA.2025.01.023 (2025) doi:10.1016/J.JMA.2025.01.023.
8. Shahsanaei, M. *et al.* Effect of nanostructured MgO directly grown on pure magnesium substrate on its in vitro corrosion and bioactivity behaviour. *Journal of Magnesium and Alloys* https://doi.org/10.1016/J.JMA.2025.05.006 (2025) doi:10.1016/J.JMA.2025.05.006.

9. Pan, S. Q., Zhang, F., Wen, C. & Zeng, R. C. Advances in Mg–Al-layered double hydroxide steam coatings on Mg alloys: A review. *Journal of Magnesium and Alloys* **11**, 1505–1518 (2023).

10. Peng, F. *et al.* Sealing the Pores of PEO Coating with Mg-Al Layered Double Hydroxide: Enhanced Corrosion Resistance, Cytocompatibility and Drug Delivery Ability. *Scientific Reports 2017 7:1* **7**, 8167- (2017).

11. Aliramezani, R., Raeissi, K., Labbaf, S. & Hakimizad, A. In-situ incorporation of polydopamine surface modified bioactive glass nanoparticles into a plasma electrolytic oxidation coating on biodegradable AZ31 Mg alloy: A study of bioactivity and corrosion performance. *J. Alloys Compd.* **1005**, 176145 (2024).

12. Heydarian, A., Rahmati, M., Atapour, M., Hakimizad, A. & Raeissi, K. Effect of electrochemical parameters on wear and tribocorrosion capabilities of the PEO coatings generated through pulsed waveforms on AZ91 magnesium alloy. *Journal of Materials Research and Technology* **27**, 6148–6158 (2023).

13. Akbarzadeh, S. *et al.* Self-healing plasma electrolytic oxidation (PEO) coating developed by an assembly of corrosion inhibitive layer and sol-gel sealing on AA2024. *Corros. Sci.* **222**, 111424 (2023).

14. del Olmo, R. *et al.* Hybrid PEO/sol-gel coatings loaded with Ce for corrosion protection of AA2024-T3. *Prog. Org. Coat.* **182**, 107667 (2023).

15. Telmenbayar, L., Ramu, A. G., Erdenebat, T. O. & Choi, D. Anticorrosive lanthanum embedded PEO/GPTMS coating on magnesium alloy by plasma electrolytic oxidation with silanization. *Mater. Today Commun.* **33**, 104662 (2022).

16. Adeleke, S. A. & Caldona, E. B. Plasma electrolytic oxidation based superhydrophobic coatings: fabrication, rudiments, and constraints. *J. Coat. Technol. Res.* **22**, 17–32 (2024).

17. Peng, F. *et al.* Sealing the Pores of PEO Coating with Mg-Al Layered Double Hydroxide: Enhanced Corrosion Resistance, Cytocompatibility and Drug Delivery Ability. *Scientific Reports 2017 7:1* **7**, 1–12 (2017).

18. Shulha, T. *et al.* LDH sealing for PEO coated friction stir welded AZ31/AA5754 materials. *Nano Materials Science* **6**, 428–442 (2024).

19. Zhang, G. *et al.* Active corrosion protection by a smart coating based on a MgAl-layered double hydroxide on a cerium-modified plasma electrolytic oxidation coating on Mg alloy AZ31. *Corros. Sci.* **139**, 370–382 (2018).

20. Zhang, G. *et al.* In-situ LDHs growth on PEO coatings on AZ31 magnesium alloy for active protection: Roles of PEO composition and conversion solution. *Journal of Magnesium and Alloys* **11**, 2376–2391 (2023).

21. Alves, A. C., Criado, D., da Silva Pereira, J. A., de Oliveira, M. C. L. & Antunes, R. A. Graphite Oxide-Based Coatings on ZK60A Magnesium Alloy: Effect of Chitosan and Silane Coupling Agents on the Corrosion Resistance. *J. Mater. Eng. Perform.* 1–15 (2024) doi:10.1007/S11665-024-09907-4/FIGURES/12.

22. Parichehr, R., Dehghanian, C. & Nikbakht, A. Preparation of PEO/silane composite coating on AZ31 magnesium alloy and investigation of its properties. *J. Alloys Compd.* **876**, 159995 (2021).

23. Fattah-alhosseini, A., Fardosi, A., Karbasi, M. & Kaseem, M. Advancements in enhancing corrosion protection of Mg alloys: A comprehensive review on the synergistic effects of combining inhibitors with PEO coating. *Journal of Magnesium and Alloys* **12**, 465–489 (2024).

24. Lu, X., Zuo, Y., Zhao, X. & Tang, Y. The improved performance of a Mg-rich epoxy coating on AZ91D magnesium alloy by silane pretreatment. *Corros. Sci.* **60**, 165–172 (2012).

25. Killian, M. S. *et al.* Interface Chemistry and Molecular Bonding of Functional Ethoxysilane-Based Self-Assembled Monolayers on Magnesium Surfaces. *ACS Appl. Mater. Interfaces* **7**, 9006–9014 (2015).

26. Talha, M. *et al.* Recent Advancements in Corrosion Protection of Magnesium Alloys by Silane-Based Sol-Gel Coatings. *Ind. Eng. Chem. Res.* **59**, 19840–19857 (2020).

27. Marcoen, K., Gauvin, M., De Strycker, J., Terryn, H. & Hauffman, T. Molecular Characterization of Multiple Bonding Interactions at the Steel Oxide-Aminopropyl triethoxysilane Interface by ToF-SIMS. *ACS Omega* **5**, 692–700 (2020).

28. Marchfelder, C., Wallner, G. M., Reischauer, M., Leidlmair, D. & Strauß, B. Effect of corrosion inhibitor modified silane pretreatment on the performance of electrical steel sheets and laminates. *Int. J. Adhes. Adhes.* **140**, 104010 (2025).

29. Su, H. Y., Chen, P. L. & Lin, C. S. Sol–gel coatings doped with organosilane and cerium to improve the properties of hot-dip galvanized steel. *Corros. Sci.* **102**, 63–71 (2016).

30. Telmenbayar, L., Gopal Ramu, A., Yang, D. & Choi, D. Development of mechanically robust and anticorrosion slippery PEO coating with metal–organic framework (MOF) of magnesium alloy. *Chemical Engineering Journal* **458**, 141397 (2023).

31. Chen, Q. *et al.* Formation of self-healing PEO coatings on AM50 Mg by in-situ incorporation of zeolite micro-container. *Corros. Sci.* **209**, 110785 (2022).

32. Yang, S., Sun, R. & Chen, K. Self-healing performance and corrosion resistance of phytic acid/cerium composite coating on microarc-oxidized magnesium alloy. *Chemical Engineering Journal* **428**, 131198 (2022).

33. Zhang, G. *et al.* Corrosion protection properties of different inhibitors containing PEO/LDHs composite coating on magnesium alloy AZ31. *Scientific Reports 2021 11:1* **11**, 2774- (2021).

34. Hernández-Barrios, C. A., Cuao, C. A., Jaimes, M. A., Coy, A. E. & Viejo, F. Effect of the catalyst concentration, the immersion time and the aging time on the morphology, composition and corrosion performance of TEOS-GPTMS sol-gel coatings deposited on the AZ31 magnesium alloy. *Surf. Coat. Technol.* **325**, 257–269 (2017).

35. Shahsanaei, M. *et al.* Synergistic enhancement of photocatalytic hydrogen production in TiO2 nanosheets through light-induced defect formation and Pt single atoms. *J. Mater. Chem. A Mater.* https://doi.org/10.1039/d4ta01809e (2024) doi:10.1039/d4ta01809e.

36. Guerra-Mutis, M. H., Vega, J. M., Barrena, M. I., Matykina, E. & Arrabal, R. Flash-PEO of magnesium: Phosphate precursor driven functionalization. *Journal of Magnesium and Alloys* **13**, 592–612 (2025).

37. Kamil, M. P., Kaseem, M. & Ko, Y. G. Soft plasma electrolysis with complex ions for optimizing electrochemical performance. *Scientific Reports 2017 7:1* **7**, 1–15 (2017).

38. Rogov, A. B., Nemcova, A., Hashimoto, T., Matthews, A. & Yerokhin, A. Analysis of electrical response, gas evolution and coating morphology during transition to soft sparking PEO of Al. *Surf. Coat. Technol.* **442**, 128142 (2022).

39. Curran, J. A. & Clyne, T. W. The thermal conductivity of plasma electrolytic oxide coatings on aluminium and magnesium. *Surf. Coat. Technol.* **199**, 177–183 (2005).

40. Cui, L. Y. *et al.* Corrosion resistance of a self-healing micro-arc oxidation/polymethyltrimethoxysilane composite coating on magnesium alloy AZ31. *Corros. Sci.* **118**, 84–95 (2017).

41. Ciobotaru, I. A. *et al.* The determination of the optimum hydrolysis time for silane films deposition. *Appl. Surf. Sci.* **371**, 275–280 (2016).

42. Tan, G., Zhang, L., Ning, C., Liu, X. & Liao, J. Preparation and characterization of APTES films on modification titanium by SAMs. *Thin Solid Films* **519**, 4997–5001 (2011).

43. Yang, J., Zuo, W., Wu, Z. & She, W. Towards a deeper understanding of the impact of tetraethoxysilane (TEOS) on early-age cement hydration. *Constr. Build. Mater.* **450**, 138624 (2024).

44. Galio, A. F. *et al.* Inhibitor-doped sol–gel coatings for corrosion protection of magnesium alloy AZ31. *Surf. Coat. Technol.* **204**, 1479–1486 (2010).

45. Li, J., Bai, H. & Feng, Z. Advances in the Modification of Silane-Based Sol-Gel Coating to Improve the Corrosion Resistance of Magnesium Alloys. *Molecules 2023, Vol. 28, Page 2563* **28**, 2563 (2023).

46. Hashemi, M. M., Hahseminia, F. & Sadeghzadeh, S. Alkyd coated laser induced graphene patches for corrosion resistance of metal substrates. *Scientific Reports 2025 15:1* **15**, 31453- (2025).

47. Zschach, L. G. *et al.* Understanding the Role of Superhydrophobicity and Superhydrophilicity in Salt-Spray Corrosion of Nanosecond Pulsed Laser-Textured AA2024 Alloy. *Adv. Funct. Mater.* e30465 (2026) doi:10.1002/ADFM.202530465;SUBPAGE:STRING:FRAMEDPDF;JOURNAL:JOURNAL:10990712;PAGE:STRING:ARTICLE/CHAPTER.

48. Ramezanzadeh, B., Ahmadi, A. & Mahdavian, M. Enhancement of the corrosion protection performance and cathodic delamination resistance of epoxy coating through treatment of steel substrate by a novel nanometric sol-gel based silane composite film filled with functionalized graphene oxide nanosheets. *Corros. Sci.* **109**, 182–205 (2016).

49. Neumann, A. W., Good, R. J., Hope, C. J. & Sejpal, M. An equation-of-state approach to determine surface tensions of low-energy solids from contact angles. *J. Colloid Interface Sci.* **49**, 291–304 (1974).

50. Young, T. III. An essay on the cohesion of fluids. *Philos. Trans. R. Soc. Lond.* **95**, 65–87 (1805).

51. Kamil, M. P., Kaseem, M., Lee, Y. H. & Ko, Y. G. Microstructural characteristics of oxide layer formed by plasma electrolytic oxidation: Nanocrystalline and amorphous structures. *J. Alloys Compd.* **707**, 167–171 (2017).

52. Zhang, D. *et al.* Effects of 8-HQ Synergistic Modification Micro-Arc Oxidation-Silane Composite Coating on the Corrosion Resistance of LA141 Alloy. *JOM 2026* 1–9 (2026) doi:10.1007/s11837-026-08188-7.

53. Qian, K. *et al.* Corrosion prevention for PEO-coated Mg by phosphate-based sealing treatment with added cation. *Appl. Surf. Sci.* **629**, 157351 (2023).

54. Berdimurodov, E. *et al.* 8–Hydroxyquinoline is key to the development of corrosion inhibitors: An advanced review. *Inorg. Chem. Commun.* **144**, 109839 (2022).

55. Alhendal, A. Enhanced thermomechanical properties of epoxy-multiwalled CNT nano-composites. *RSC Adv.* **14**, 35360–35372 (2024).

56. Ou, G. P., Gui, W. M., Jin, S. C. & Zhang, F. J. Surface analysis for LiBq4 growing on ITO and CuPc film using atomic force microscopy (AFM) and X-ray photoelectron spectroscopy (XPS). *Appl. Surf. Sci.* **252**, 3417–3427 (2006).

57. Tang, L., Li, X., Si, Y., Mu, G. & Liu, G. The synergistic inhibition between 8-hydroxyquinoline and chloride ion for the corrosion of cold rolled steel in 0.5 M sulfuric acid. *Mater. Chem. Phys.* **95**, 29–38 (2006).

58. Shen, S., Zuo, Y. & Zhao, X. The effects of 8-hydroxyquinoline on corrosion performance of a Mg-rich coating on AZ91D magnesium alloy. *Corros. Sci.* **76**, 275–283 (2013).

59. Toorani, M., Aliofkhazraei, M., Mahdavian, M. & Naderi, R. Effective PEO/Silane pretreatment of epoxy coating applied on AZ31B Mg alloy for corrosion protection. *Corros. Sci.* **169**, 108608 (2020).

60. Chaudry, U. M. *et al.* Corrosion Behavior of AZ31 and AZ31-0.5Ca in Different Concentrations of NaCl and Na2SO4 at Various Temperatures. *Corrosion* **81**, 232–244 (2025).

61. Jamshidipour, Z., Toorani, M., Aliofkhazraei, M. & Mahdavian, M. Reducing damage extent of epoxy coating on magnesium substrate by Zr-enhanced PEO coating as an effective pretreatment. *Journal of Magnesium and Alloys* **11**, 641–656 (2023).

62. Gobara, M., Baraka, A., Akid, R. & Zorainy, M. Corrosion protection mechanism of Ce4+/organic inhibitor for AA2024 in 3.5% NaCl. *RSC Adv.* **10**, 2227–2240 (2020).

63. Patra, R., Vijay, B., Raju, K. R. C. S., Gobi, K. V. & Subasri, R. Dual functional coatings: Comparative study of corrosion indicators for corrosion reporting and self-healing on MgAZ31 alloy. *J. Alloys Compd.* **1029**, 180755 (2025).

64. Vaghefinazari, B. *et al.* Exploring the corrosion inhibition mechanism of 8-hydroxyquinoline for a PEO-coated magnesium alloy. *Corros. Sci.* **203**, 110344 (2022).

65. Chen, D. *et al.* Protective nature of cerium-based oxides coating against Mg corrosion in Hanks' balanced salt solution. *Corros. Sci.* **219**, 111255 (2023).

Supplementary Files

This is a list of supplementary files associated with this preprint. Click to download.

- AZ31Supportinformation.docx
- GraphicalAbstract.tiff